Multifacet structure of observed reconstructed integral images

Manuel Martínez-Corral* and Bahram Javidi

Electrical and Computer Engineering Dept., University of Connecticut, Storrs, Connecticut 06269-1157

Raúl Martínez-Cuenca and Genaro Saavedra

Department of Optics, University of Valencia, E46100 Burjassot, Spain

Received July 30, 2004; accepted October 4, 2004

Three-dimensional images generated by an integral imaging system suffer from degradations in the form of grid of multiple facets. This multifacet structure breaks the continuity of the observed image and therefore reduces its visual quality. We perform an analysis of this effect and present the guidelines in the design of lenslet imaging parameters for optimization of viewing conditions with respect to the multifacet degradation. We consider the optimization of the system in terms of field of view, observer position and pupil function, lenslet parameters, and type of reconstruction. Numerical tests are presented to verify the theoretical analysis.

OCIS codes: 110.6880, 110.4190, 120.2040.

1. INTRODUCTION

Currently much visual information is presented to users through computer monitors, TV screens, and even cellular-phone or personal data assistant screens. The displayed images can have entertainment or information value or even be aimed at the diffusion of scientific results.[1] The information society increasingly demands the display not only of plane images but also of three-dimensional (3D) images or even movies,[2–5] with continuous perspective information. Although the search for optimum 3D imaging and display techniques has been the subject of research for more than a century,[6] only in the past few years has technology approached the level required for realization of 3D imaging systems. So-called integral imaging (II), which is a 3D imaging technique especially suited to the above requirements, works with incoherent light and provides autostereoscopic images without the help of special glasses. In an II system, an array of microlenses generates onto a sensor such as a CCD a collection of plane elemental images. Each elemental image has a different perspective of the 3D object, and therefore the CCD records tomographical information of the object. In the reconstruction stage, the recorded images are displayed by an optical device, such as a liquid-crystal device (LCD) monitor, placed in front of another microlens array. This setup provides the observer with a reconstructed 3D image with full paralax. Integral imaging was first proposed by Lippmann,[7] and some relevant work has been done since then.[8–12] The interest in II has been resurrected recently because of its application to 3D TV and display.[13]

Since its rebirth, II has overcome many of its challenges. Specifically, it is notable that a simple technique for pseudoscopic to orthoscopic conversion has been developed.[14] Some methods have been proposed to overcome the limits in lateral resolution imposed by the pixelated structure of the CCD[15–17] or by the microlens array.[18,19] Other challenges that have been satisfactorily faced are the enhancement of the depth of field[20,21] and of the viewing area.[22] Apart from this engineering work, some purely theoretical work has also been performed to characterize the resolution response of II systems[23,24] or the viewing parameters in the display stage.[25]

However, it is somewhat surprising that, in spite of the intense research effort carried out in the past few years, no study (as far as we know) has been devoted to a phenomenon that is indeed present in many of the reported experiments and that reduces significantly the visual quality of the reconstructed image when the image is finally seen by the observer. We refer to the multifacet structure of the observed image. Such a structure appears as a result of an inappropriate overlapping between the elemental fields of view (FOVs) provided by the different microlenses.

The FOV of an optical system is the extent of the object plane that is imaged by the system. In II, the final FOV is the result of a three-step process. In the pickup the FOV, as expressed in angular units, is given by $\psi = \arctan(\phi/2f)$, where ϕ is the diameter of the lenslets and f is their focal length.[9] If the display setup is arranged correctly, the scale and FOV of reconstructed image are the same as those of the object.[26] However, when the reconstructed image is seen by the observer, a new stop is incorporated to the system: the eye pupil. Depending on the system geometry, this stop can act as the exit pupil or as the exit window. In both cases a harmful limitation of the FOV appears that, owing to its multifacet structure, degrades the quality of the image.

The aim of this paper is to provide a theoretical analysis of the multifacet structure of the observed reconstructed image. We will analyze two kinds of reconstruction geometries and will determine the optimum

arrangement that eliminates the multifacet effect. The paper is organized as follows. In Section 2 we review the principles of integral imaging pickup and the different types of reconstruction: real pseudoscopic or virtual orthoscopic. In Section 3 we develop the geometrical theory of multiple elemental FOVs in the case of real pseudoscopic reconstruction. Section 4 is devoted to the case of the virtual orthoscopic reconstruction. Finally, in Section 5 we outline the main achievements of this work.

2. PRINCIPLE OF INTEGRAL IMAGING

Consider the pickup stage of an II system as shown in Fig. 1. The system is adjusted so that a representative plane of the object area, named here the reference object plane, and the pickup plane are conjugated through the microlenses. Then distances d and g are related by the lens law, $1/g + 1/d = 1/f$, f being the lenslets' focal length. The lateral magnification between the reference plane and the pickup plane is

$$M_p = -\Delta/f, \quad \text{where } \Delta = g - f = f^2/(d - f). \quad (1)$$

The lenslets' diameter is denoted by ϕ_L, and the pitch is denoted by p. In general ϕ_L and p are different; therefore we define the microlenses' fill factor as $\varphi = \phi_L/p$. During the pickup, the light scattered at the surface of the 3D object generates a collection of elemental two-dimensional (2D) images onto the pickup device (CCD). Each elemental image has a different perspective of the 3D object. Rays proceeding from object points in the reference plane intersect fully at the pickup plane, allowing the capture of sharp images. In contrast, rays proceeding from object points outside of the reference plane intersect not in the pickup plane but in its neighborhood, giving rise to the capture of blurred images. This blurring is primarily responsible for the limited depth of field of II systems. Several techniques have been reported recently to reduce the pickup blurring.[21,27] To derive a rigorous expression of the intensity distribution generated at the pickup plane, $I(\mathbf{x}')$, it is necessary to apply the scalar paraxial diffraction equations, according to Ref. 21:

$$I(\mathbf{x}') = \int_{R^2} R(\mathbf{x}) H[\mathbf{x}';\, \mathbf{x},\, z = f(\mathbf{x})]\, \mathrm{d}^2\mathbf{x}, \quad (2)$$

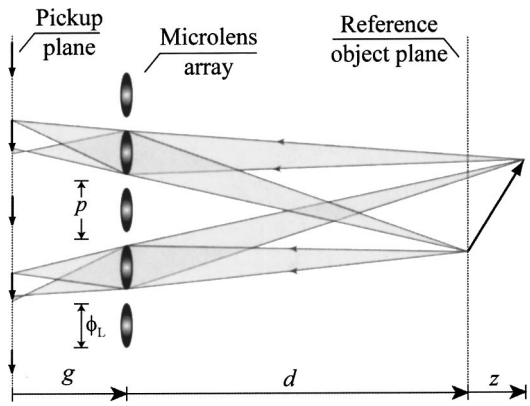

Fig. 1. Schematic drawing, not to scale, of the pickup stage of an integral imaging system. Each elemental image has a different perspective of the object. Object points out of the reference plane produce blurred images onto the CCD.

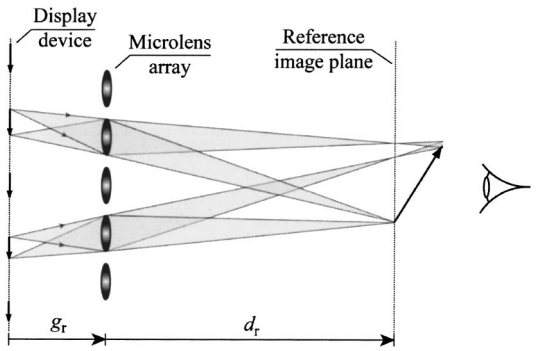

Fig. 2. Schematic drawing of pseudoscopic real reconstruction. The reconstructed image is depth reversed from the observer point of view. Object points at the reference plane are sharply reconstructed.

where

$$H(\mathbf{x}';\, \mathbf{x},\, z) = H_o(\mathbf{x}';\, z) \otimes \sum_{\mathbf{m}} \delta\{\mathbf{x}' - [\mathbf{m}p(1 - M_z) - M_z\mathbf{x}]\}. \quad (3)$$

Here $\delta(\cdot)$ is the Dirac delta function, $\otimes$ denotes the 2D convolution product, and

$$H_o(\mathbf{x}';\, z) = \left| \int_{R^2} p(\mathbf{x_o}) \exp\left(-i \frac{\pi z}{\lambda d(d + z)} |\mathbf{x_o}|^2 \right) \times \exp\left(-i 2\pi \mathbf{x_o} \frac{\mathbf{x}'}{\lambda g} \right) \mathrm{d}^2\mathbf{x_o} \right|^2. \quad (4)$$

In the above equations, $\mathbf{m} = (m, n)$ accounts for the microlenses' indices in the (x, y) directions, $M_z = -g/(d + z)$ is the lateral magnification, $p(\mathbf{x_o})$ is the lenslets' pupil function, $R(\mathbf{x})$ accounts for the object intensity reflectivity, and $f(\mathbf{x}) - z = 0$ is the function that describes the surface of the 3D object.

As for the reconstruction process, primarily two types of architecture have been reported. In one case, the recorded 2D elemental images are displayed by an optical device (such as a LCD) placed in front of another microlens array. If a reconstructed image of the same size and position as the original object is the aim, the display lenslet array should have the same pitch and focal length as the pickup one.[26] The LCD and the microlens array are adjusted so that the distance between them, g_r, is the same as the pickup gap, g. As shown in Fig. 2, this architecture permits the reconstruction of a real image at a distance $d_r = d$. The lateral magnification between the display-device plane and the reference image plane is $M_r = -f/\Delta$, Δ being the parameter defined in Eq. (1). Then the overall lateral magnification of the pickup and reconstruction process is $M_T = M_p M_r = 1$. Object points in the reference plane are sharply reconstructed. In contrast, the reconstructed images of object points outside the reference plane are blurred even if neither the pickup blurring nor the pixelation effect has been taken into account. The main drawback of this architecture is that the reconstructed image is pseudoscopic; i.e., it is depth reversed from the observer point of view.

Several techniques have been proposed for producing an orthoscopic reconstruction of the 3D object.[8,11–13] The simplest one is shown in Fig. 3. In this architecture, each elemental image is rotated 180° around the center of the elemental cell. To get the same lateral magnification as in the pseudoscopic reconstruction but with different sign, the gap is reduced to

$$g_v = g - 2\Delta = g - 2\frac{f^2}{d - f}. \tag{5}$$

As can be seen from the figure, this setup allows the one-step reconstruction of an orthoscopic virtual image of the 3D object. Now the lateral magnification between the display-device plane and the reference image plane is $M_v = f/\Delta$. The overall lateral magnification of the pickup/reconstruction process is $M_T = -M_p M_v = 1$, where the minus sign appears as a result of the 180° rotation. The reconstructed image and the object have the same scale in both the lateral and the axial directions. The reference image plane appears at a distance $d_v = d - 2f$ from the lenslet array. Note that although in some papers[25,28] it is mentioned that g_v should be smaller than g, we report for the first time, to the best of our knowledge, the exact value of g_v. In other reported studies, it is proposed to set the LCD at a distance $g_v = g$. However, such a configuration does not allow the reconstruction of sharp images but only the reconstruction of images with very poor resolution. This is because it does not permit the full intersection of rays that proceed from the elemental images.

3. MULTIFACET STRUCTURE OF THE OBSERVED PSEUDOSCOPIC IMAGE

When the observer places the eye in front of the lenslet array and looks through it to see the reconstructed image, he or she sees a different portion of the image through each lenslet. Such image portions are the elemental FOVs provided by any microlens. Depending on the system geometry, the elemental FOVs may or may not overlap, giving rise in some cases to reconstructed images divided into multiple facets. Such a multifacet structure can degrade the quality of the observed image, because it

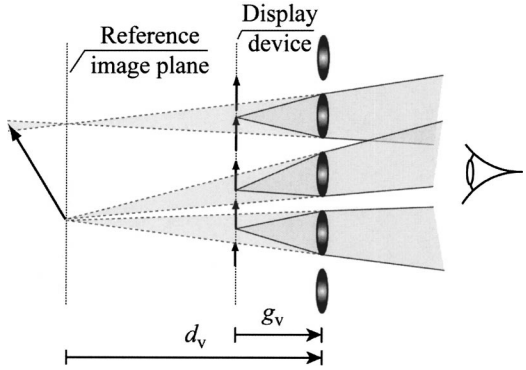

Fig. 3. Schematic drawing of orthoscopic virtual reconstruction. The gap distance is reduced to $g_v = g - 2f^2/(d - f)$. The reconstructed image and the object have the same size. Object points at the reference plane are sharply reconstructed.

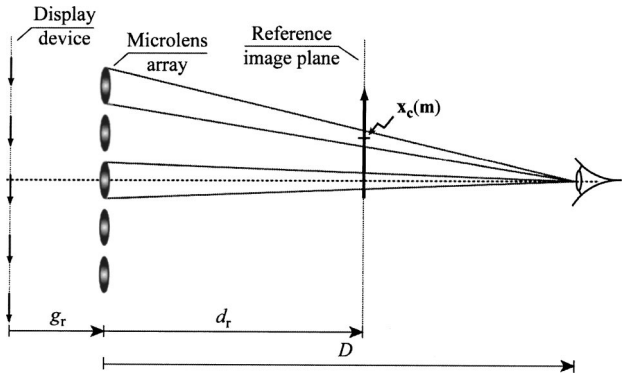

Fig. 4. Observation of the reconstructed real image. The observed image consists of a rectangular grid of elemental FOVs. Each elemental FOV is observed through a different microlens. The elemental FOVs are centered at points $\mathbf{x_c(m)}$.

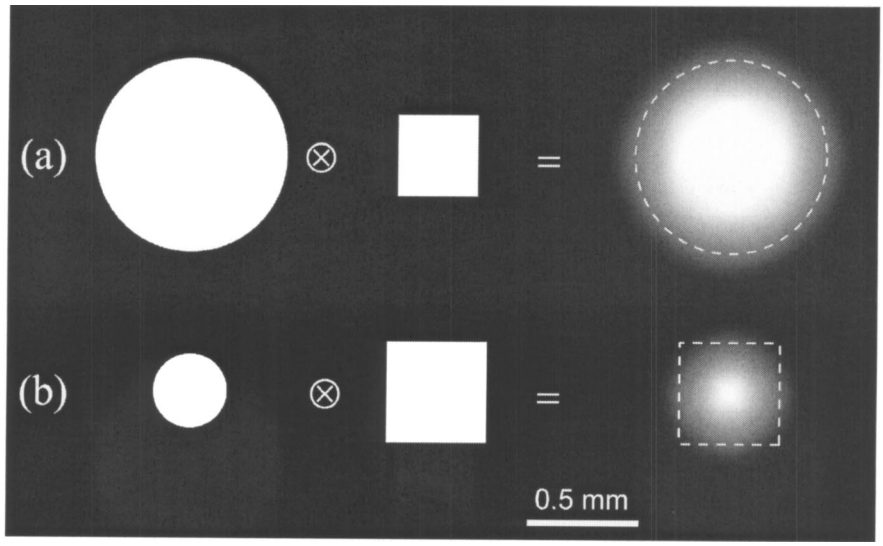

Fig. 5. Illustration of calculation of the elemental FOV function. (a) When the observer is placed at a distance $D_1 = 350$ mm from the microlenses, the FOVs have a circle-like shape; (b) when $D_2 = 900$ mm the FOVs are square like. In both cases we have marked the field of half-illumination (dashed line).

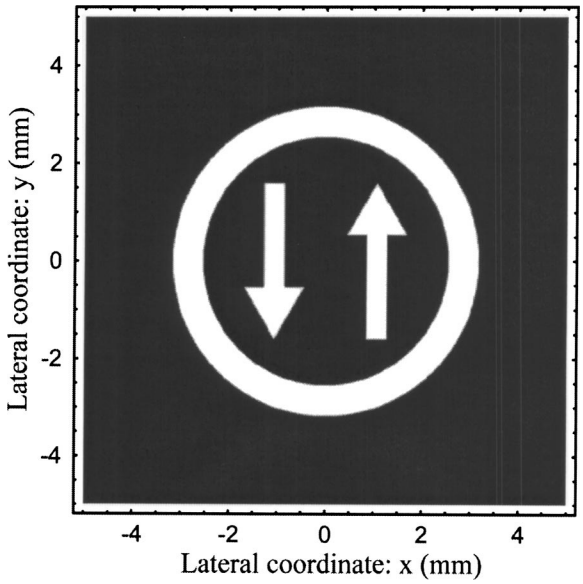

Fig. 6. Synthetic object used for the numerical experiments.

breaks the continuity of its visual aspect. In what follows, we analyze the importance of the multifacet phenomenon and the influence on it of several factors such as the observer position, the type of reconstruction, or the lenslets' fill factor.

First we address the case of real pseudoscopic reconstruction. Figure 4 shows the observation of the reconstructed image. The image is reconstructed by the superposition of projected elemental images, each with a different perspective. The observer is placed at a distance D from the microlens array. Take into account that the distance from the observer to the reconstructed image, $D - d_r$, must be larger than the nearest distance of distinct vision, which, for the case of an adult observer, is $\sim$250 mm.[29] As shown heuristically in Fig. 4, the observer's full FOV is composed of a collection of elemental FOVs arranged in a rectangular grid. Such elemental FOVs are centered at positions

$$\mathbf{x}_c(\mathbf{m}) = \frac{D - d_r}{D}\mathbf{m}p. \tag{6}$$

Although in the pickup stage it is preferable for the lenslets to be circular-shaped,[21] we will find in this paper that in the display stage it is much more preferable to proceed with square-shaped lenslets. Thus in what follows we consider that the lenslets are square shaped with side Δ_L. The observer-eye entrance pupil is circular with diameter ϕ_E. Then the elemental FOVs' shape results from the convolution between two projected pupils: (a) the projection, through the eye-pupil center, of the lenslet pupil onto the image plane and (b) the projection, through the lenslet center, of the eye pupil onto the image plane.[30] Then the elemental FOVs are expressed as

$$E(\mathbf{x}) = \mathrm{rect}\left(\frac{\mathbf{x}}{w}\right) \otimes \mathrm{circ}\left(2\frac{\mathbf{r}}{\phi}\right), \tag{7}$$

where

$$\phi = \frac{d_r}{D}\phi_E, \qquad w = \frac{D - d_r}{D}\Delta_L. \tag{8}$$

Since the elemental FOVs are obtained as the result of the convolution between two binary functions, they are no longer binary. Specifically, they consist of a central zone with uniform FOV and an outer zone of vigneting where the illumination falls off gradually. For distances D larger than the distance D_ϕ, defined as

$$D_\phi = d_r\frac{\phi_\mathrm{E} + \Delta_\mathrm{L}}{\Delta_\mathrm{L}}, \tag{9}$$

the eye pupil acts as the exit pupil of the system, and the lenslet acts as the exit window. Thus the elemental

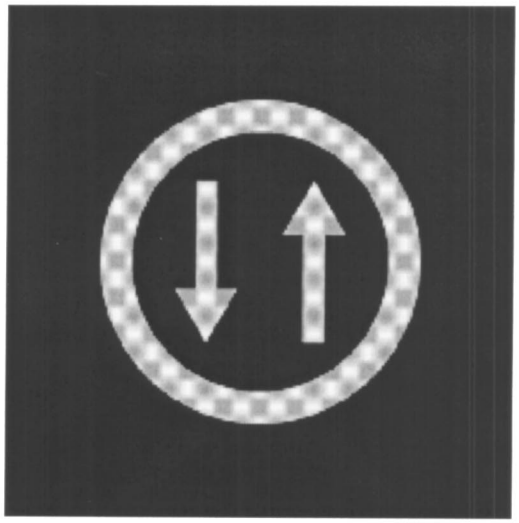

(a)

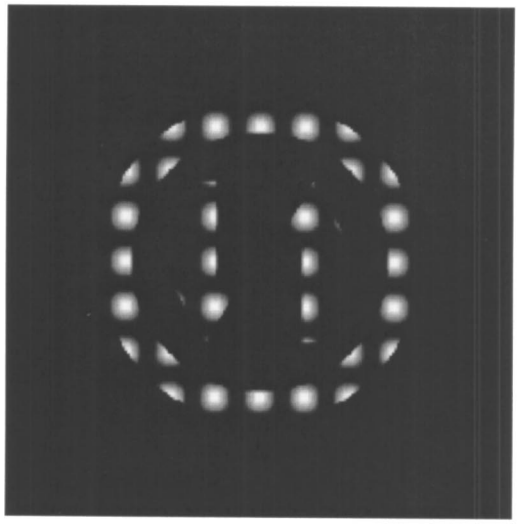

(b)

Fig. 7. For the case of $\varphi = 0.5$: (a) reconstructed image as seen by the observer when distance is set at $D_1 = 350$ mm, (b) reconstructed image as seen by the observer when $D_2 = 900$ mm.

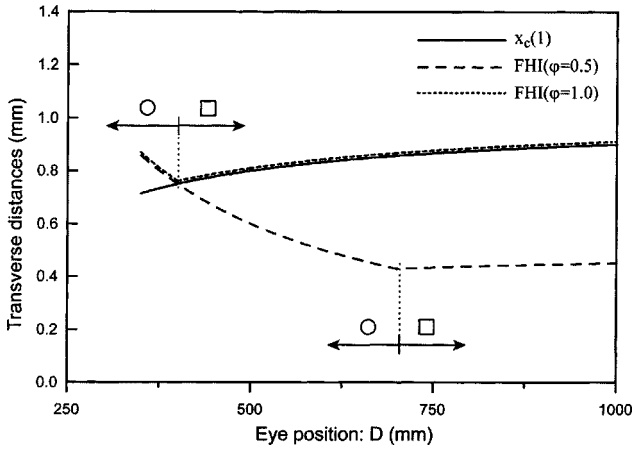

Fig. 8. Variation with D of spacing between adjacent FOVs (solid curve) and of the FHI. The curves start at the nearest distance of distinct vision. For $D < D_\phi$ the FOVs have circle-like shape. For $D > D_\phi$ they have square-like shape.

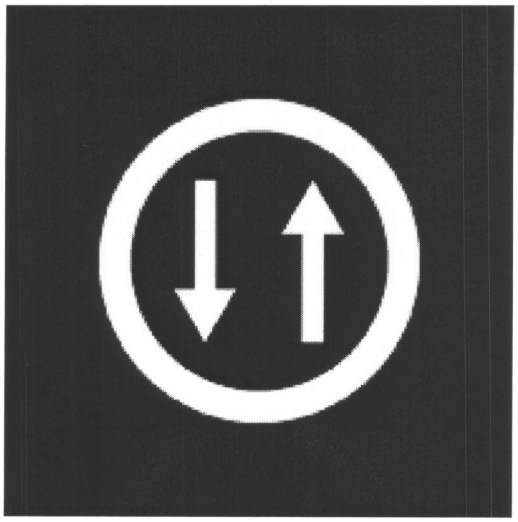

Fig. 9. For the case of $\varphi = 1.0$, the reconstructed image as seen by the observer when set, for example, at $D = 350$ mm. Note that in this case the visual aspect of the observed image is independent of the value of D.

FOVs have a square-like shape. In contrast, for eye positions such that $D < D_\phi$, the eye pupil acts as the exit window, and therefore the elemental FOVs have a circle-like shape. In Fig. 5 we show the elemental FOV function, $E(\mathbf{x})$, corresponding to two different values of D. For calculation we assumed a typical integral-image setup, that is, $f = 5.0$ mm, $p = 1.0$ mm, $d = d_r = 100$ mm, and $\phi_E = 3.0$ mm. We considered the case in which the fill factor is $\varphi = 0.5$.

To perform the analysis in the simplest way, we considered, as drawn in Fig. 4, a plane object, which can be described by the function $O(\mathbf{x})$. Since the image is reconstructed with magnification equal to one, it can be described by the same function $O(\mathbf{x})$.[31] The reconstructed image as seen by the observer, i.e., the observed reconstructed image ORI($\mathbf{x}$), is obtained as the linear superposition of the array of elemental FOVs, that is,

$$\mathrm{ORI}(\mathbf{x}) = \sum_{\mathbf{m}} \{O(\mathbf{x})E[\mathbf{x} - \mathbf{x_c}(\mathbf{m})]\}. \tag{10}$$

In Fig. 6 we show the synthetic object used in our numerical experiments. This figure also represents the reconstructed image. By use of Eqs. (6)–(10), we calculated the reconstructed images as seen by the observer when positioned at distances $D_1 = 350$ mm, which corresponds to the nearest distance of distinct vision, and $D_2 = 900$ mm. The images are shown in Fig. 7. The quality is rather poor owing to the multifacet structure. To better understand the reason for this structure, it is convenient to compare the function $\mathbf{x_c}(1)$, defined in Eq. (6) and which determines the spacing between adjacent elemental FOVs, and the field of half-illumination (FHI), which determines the elemental FOVs' size. In this system the FHI is calculated as

$$\mathrm{FHI}(D) = \max\{\phi, w\}, \tag{11}$$

where ϕ and w are defined in Eq. (8). As shown in Fig. 8, the spacing between adjacent FOVs gradually increases as the observer moves away from the lenslet array (solid curve). The FOVs' size (long-dashed curve) is much smaller than the spacing over almost the whole range of possible observer positions. $D_\phi = 700$ mm appears to be the border between positions where the elemental FOVs' have circle-like shape and positions where they have square-like shape. It is evident from the graph that at $D_2 = 900$ mm the elemental-FOVs' spacing is twice their size, so that there is no overlapping between the elemental FOVs. Consequently, the observed image has multifacet structure with large black areas between the facets. In the case of $D_1 = 350$ mm, the FOVs' spacing is slightly smaller than their size, and therefore the elemental FOVs do overlap. However, since now the elemental FOVs have circle-like shape but are arranged in a rectangular grid, the observed image still shows a multifacet structure.

In Fig. 8 we have also plotted the evolution of the FHI for the case of $\varphi = 1.0$ (see the short-dashed curve). Now the optimum overlap takes place for almost the entire eye-position range. The overlap is optimum when the following two conditions are satisfied: (a) The values for $\mathbf{x_c}(1)$ and FHI are equal, and (b) the elemental FOVs have square-like form. In Fig. 9 we show the reconstructed images as seen by the observer when positioned at distance $D = 350$ mm. Note that now the observed image no longer has a multifacet structure. We can conclude at this point that although the use of display microlenses with low fill factor has been proposed in some studies to increase the depth of field or the viewing angle, it degrades the quality of observed images owing to the facet pattern. The multifacet effect can be reduced by use of the moving-array lenslet technique.[18,19]

4. VIRTUAL ORTHOSCOPIC RECONSTRUCTION

In Fig. 10 we present the observation of the reconstructed virtual orthoscopic image. The observer is placed at a distance D from the microlenses such that the distance to the reconstructed image, $D + d_v$, is larger than the nearest distance of distinct vision. As in the previous case

the observed full FOV consists of a rectangular grid of elemental FOVs, which are now centered at points

$$\mathbf{x}_c(\mathbf{m}) = \frac{D + d_v}{D}\mathbf{m}p. \tag{12}$$

Again, the shape of the elemental FOV, $E(\mathbf{x})$, results from the convolution between a square and a circle. In this case, their diameter and width are

$$\phi = \frac{d_v}{D}\phi_E \quad \text{and} \quad w = \frac{D + d_v}{D}\Delta_L, \tag{13}$$

respectively. The distance D_ϕ at which the shape of the FOV switches from circular to square is given by

$$D_\phi = d_v\frac{\phi_E - \Delta_L}{\Delta_L}. \tag{14}$$

In Fig. 11 we compare the spacing between adjacent FOVs with the FHI for two values of the fill factor. In the case of $\varphi = 0.5$, the spacing between FOVs is much larger than their size. Then, for almost the entire range of possible eye positions, the observed image has a strong multifacet structure, which breaks the desired continuity of the observed image. This effect is seen in Fig. 12(a), where we present the observed reconstructed image for a typical observation distance, say, $D = 300$ mm. In contrast, in the case of $\varphi = 1.0$ the optimum overlap takes place again for almost the entire observer eye-position range [see, for an example, Fig. 12(b)]. In Fig. 12(c) we have presented the same observed reconstructed image but for the case in which the microlenses are circular with fill factor $\varphi = 1.0$. Note that in this case the second condition for optimum overlapping of FOVs does not hold,

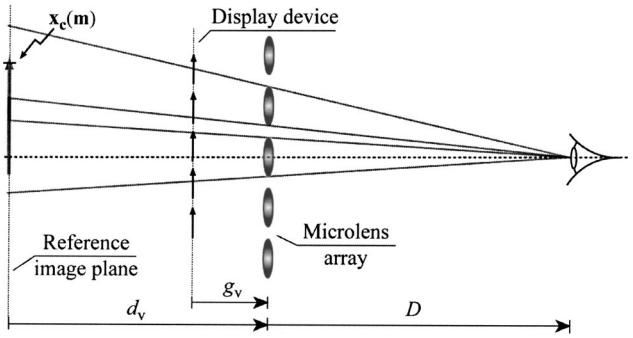

Fig. 10. Observation of reconstructed virtual image. The observed image consists of a rectangular grid of elemental FOVs, which are centered at points $\mathbf{x}_c(\mathbf{m})$.

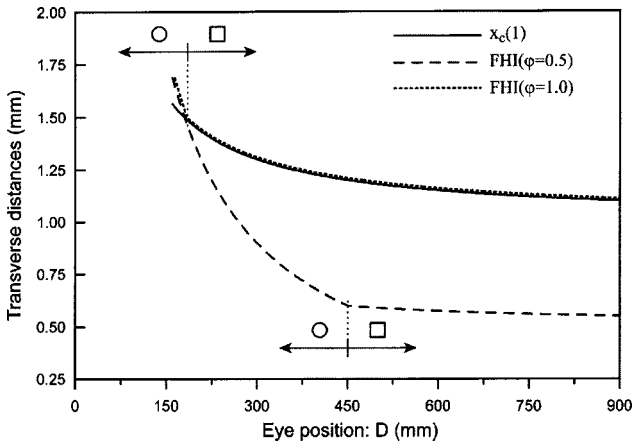

Fig. 11. Variation with D of spacing between adjacent FOVs (solid curve) and of the FHI. The curves start at the nearest distance of distinct vision.

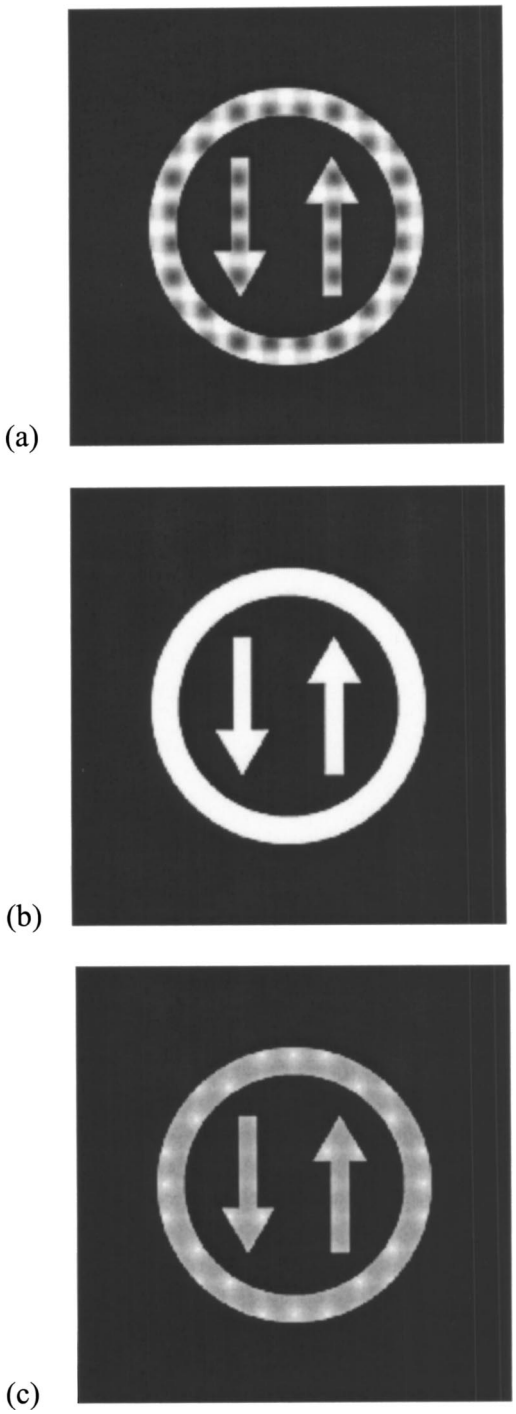

Fig. 12. Reconstructed virtual image as seen by the observer when set at $D = 300$ mm: (a) the case of square lenslets of $\varphi = 0.5$, (b) the case of square lenslets of $\varphi = 1.0$, and (c) the case of circular lenslets of $\varphi = 1.0$.

and a multifacet image appears. This is because now the elemental FOVs are circular while being arranged in a rectangular grid.

5. CONCLUSIONS

In summary, we have shown that in integral imaging, the reconstructed image as seen by the observer is a linear superposition of elemental fields of view arranged in a rectangular grid. This structure can lead, depending on the system geometry, to an observed image with a multifacet structure that breaks the continuity of the image and degrades its visual quality. We have presented an analysis for optimization in terms of field of view, observer position and pupil function; lenslet parameters, and type of reconstruction. We have shown that the optimum superposition takes place when the distance between adjacent fields of view equals their field of half-illumination and when the elemental FOVs have square-like form. This fact prevents us from using display microlenses with fill factor smaller than 1 or those with circular mount. The search for the optimum conditions when the total magnification of the integral imaging arrangement (recording + display) is different from 1 will be addressed in further research.

ACKNOWLEDGMENTS

We express our gratitude to an anonymous reviewer, whose comments and suggestions helped to improve the quality of the paper. This work has been partially funded by the Plan Nacional I+D+I (grant DPI2003-4698), Ministerio de Ciencia y Tecnología, Spain. We also acknowledge the financial support from the Generalitat Valenciana, Spain (grant grupos03/227). R. Martínez-Cuenca gratefully acknowledges financial support from the Universitat de València (Cinc Segles grant).

*Permanent address, Department of Optics, University of Valencia, E46100 Burjassot, Spain. E-mail, manuel.martinez@uv.es.

REFERENCES AND NOTES

1. J.-S. Jang and B. Javidi, "Three-dimensional integral imaging of micro-objects," Opt. Lett. **29**, 1230–1232 (2004).
2. H. Liao, M. Iwahara, N. Hata, and T. Dohi, "High-quality integral videography using a multiprojector," Opt. Express **12**, 1067–1076 (2004).
3. S. A. Benton, ed., *Selected Papers on Three-Dimensional Displays* (SPIE Optical Engineering Press, Bellingham, Wash., 2001).
4. D. H. McMahon and H. J. Caulfield, "A technique for producing wide-angle holographic displays," Appl. Opt. **9**, 91–96 (1970).
5. P. Ambs, L. Bigue, R. Binet, J. Colineau, J.-C. Lehureau, and J.-P. Huignard, "Image reconstruction using electro-optic holography," *Proceedings of the 16th Annual Meeting of the IEEE Lasers and Electro-Optics Society, LEOS 2003* (IEEE Press, Piscataway, N.J., 2003), Vol. 1, pp. 172–173.
6. T. Okoshi, "Three-dimensional displays," Proc. IEEE **68**, 548–564 (1980).
7. M. G. Lippmann, "Epreuves reversibles donnant la sensation du relief," J. Phys. (Paris) **7**, 821–825 (1908).
8. H. E. Ives, "Optical properties of a Lippmann lenticuled sheet," J. Opt. Soc. Am. **21**, 171–176 (1931).
9. C. B. Burckhardt, "Optimum parameters and resolution limitation of integral photography," J. Opt. Soc. Am. **58**, 71–76 (1968).
10. T. Okoshi, "Optimum design and depth resolution of lens-sheat and projection-type three-dimensional displays," Appl. Opt. **10**, 2284–2291 (1971).
11. N. Davies, M. McCormick, and L. Yang, "Three-dimensional imaging systems: a new development," Appl. Opt. **27**, 4520–4528 (1988).
12. N. Davies, M. McCormick, and M. Brewin, "Design and analysis of an image transfer system using microlens array," Opt. Eng. **33**, 3624–3633 (1994).
13. F. Okano, H. Hoshino, J. Arai, and I. Yayuma, "Real-time pickup method for a three-dimensional image based on integral photography," Appl. Opt. **36**, 1598–1603 (1997).
14. J. Arai, F. Okano, H. Hoshino, and I. Yuyama, "Gradient-index lens-array method based on real-time integral photography for three-dimensional images," Appl. Opt. **37**, 2034–2045 (1998).
15. L. Erdmann and K. J. Gabriel, "High-resolution digital photography by use of a scanning microlens array," Appl. Opt. **40**, 5592–5599 (2001).
16. S. Kishk and B. Javidi, "Improved resolution 3D object sensing and recognition using time multiplexed computational integral imaging," Opt. Express **11**, 3528–3541 (2003).
17. A. Stern and B. Javidi, "Three-dimensional image sensing and reconstruction with time-division multiplexed computational integral imaging," Appl. Opt. **42**, 7036–7042 (2003).
18. J.-S. Jang and B. Javidi, "Three-dimensional synthetic aperture integral imaging," Opt. Lett. **27**, 1144–1146 (2002).
19. J.-S. Jang and B. Javidi, "Improved viewing resolution of three-dimensional integral imaging by use of nonstationary micro-optics," Opt. Lett. **27**, 324–326 (2002).
20. J.-S. Jang and B. Javidi, "Large depth-of-focus time-multiplexed three-dimensional integral imaging by use of lenslets with nonuniform focal lengths and aperture sizes," Opt. Lett. **28**, 1924–1926 (2003).
21. M. Martínez-Corral, B. Javidi, R. Martínez-Cuenca, and G. Saavedra, "Integral imaging with improved depth of field by use of amplitude modulated microlens array," Appl. Opt. **43**, 5806–5813 (2004).
22. H. Choi, S.-W. Min, S. Jung, J.-H. Park, and B. Lee, "Multiple-viewing-zone integral imaging using dynamic barrier array for three-dimensional displays," Opt. Express **11**, 927–932 (2003).
23. J. Arai, H. Hoshino, M. Okui, and F. Okano, "Effects on the resolution characteristics of integral photography," J. Opt. Soc. Am. A **20**, 996–1004 (2003).
24. H. Hoshino, F. Okano, H. Isono, and I. Yuyama, "Analysis of resolution limitation of integral photography," J. Opt. Soc. Am. A **15**, 2059–2065 (1998).
25. J.-H. Park, S.-W. Min, S. Jung, and B. Lee, "Analysis of viewing parameters for two display methods based on integral photography," Appl. Opt. **40**, 5217–5232 (2001).
26. J. Arai, M. Okui, M. Kobayashi, and F. Okano, "Geometrical effects of positional errors in integral photography," J. Opt. Soc. Am. A **21**, 951–958 (2004).
27. R. Martínez-Cuenca, G. Saavedra, M. Martínez-Corral, and B. Javidi, "Enhanced depth of field integral imaging with sensor resolution constraints," Opt. Express **12**, 5237–5242 (2004).
28. J.-S. Jang and B. Javidi, "Formation of orthoscopic three-dimensional real images in direct pickup one-step integral imaging," Opt. Eng. **42**, 1869–1870 (2003).
29. D. A. Atchinson and G. Smith, *Optics of the Human Eye* (Butterworth-Heinemann, Oxford, UK, 2000).
30. M. P. Keating, *Geometric, Physical, and Visual Optics* (Butterworth-Heinemann, Oxford, UK, 1988).
31. An exact calculation would give the reconstructed image as the convolution between $O(\mathbf{x})$ and a properly scaled version of the self-convolution of function $\mathbf{H}_{\circ}(\mathbf{x}; 0)$. Since the study of resolution is not the aim of this paper, the following calculations can be accurately performed by assuming non-significant differences between the object and the reconstructed image.